Surface roughness-induced absorption acts as an ovarian cancer cells growth sensor-monitor

Aviad Katiyi [a,b], Jonathan Zorea [c], Aviran Halstuch [a,b], Moshe Elkabets [c], Alina Karabchevsky [a,b,*]

[a] School of Electrical and Computer Engineering, Ben-Gurion University of the Negev, Beer-Sheva, 8410501, Israel
[b] Ilse Katz Institute for Nanoscale Science & Technology, Ben-Gurion University of the Negev, Beer-Sheva 8410501, Israel
[c] The Shraga Segal Department of Microbiology, Immunology and Genetics, Faculty of Health Sciences, Ben-Gurion University of the Negev, Beer-Sheva, 8410501, Israel

ARTICLE INFO

ABSTRACT

Uncontrolled growth of ovarian cancer cells is the fifth leading cause of female cancer deaths since most ovarian cancer patients are diagnosed at an advanced stage of metastatic disease. Here, we report on the sensor for monitoring the cancer treatment efficiency in real-time. We measure the optical interaction between the evanescent fields of microfiber and ovarian cancer inter-cellular medium at different treatment stages. Spectral absorption signatures are correlated with optical micrographs and western blot tests. We found that the treatment of tumor cells with induces both cells growth arrest and alter the spectral lines in a dose-dependent manner. These observations are mediated by surface roughness out of silica glass material, form an essential step toward the development of early detection of response to cancer therapy.

1. Introduction

Ovarian cancer is the fifth leading cause of female cancer deaths due to late stage diagnoses (Fishman and Bozorgi, 2002; Lengyel, 2010), while diagnosis at earlier stages of ovarian cancer has a 5-year relative survival rate of 92% (Noone et al., 2018). However, most ovarian cancer patients are diagnosed at an advanced stage of metastatic disease, as the tumor spreads into the peritoneum. This aggressive disease is incurable and the survival rate of such a patient is as low as 30%. This poor survival rate is primarily related to recurrent disease of chemotherapy-resistant tumors, hence, adjustment of an appropriate second and third line of chemotherapy (or targeted therapy) is required to improve the survival rate. Currently, there are no clinical biomarkers to prioritize treatment for these patients (except of BRCA1/2 mutation (Kurian et al., 2010; Lee et al., 2013)), and treatment efficiency is monitored weeks after the initial treatment. Application of a system that will record therapy efficiency hours or days after treatment will be a major milestone in the care of ovarian cancer patients.

The conventional procedure of monitoring cancer treatment efficiency is performed with harmful methods such as positron emission tomography (PET) and computed tomography (CT) scan simultaneously (Beyer et al., 2000; Johnson et al., 2016; Fischer et al., 2009; Pelosi et al., 2004). The PET scan gives information about the activity of the cell using a radioactive tracer, while the CT scan gives a 3-dimensional image of the body using X-ray. Simultaneous PET–CT monitoring provides an accurate information about the tumor morphology and malignancy state (Schäfers and Stegger, 2008; Stegger et al., 2007). However, this not-affordable, bulky, and cumbersome imaging equipment is both harmful and not suitable for bedside monitoring; it is not always available and requires qualified personnel to operate.

Silica glass is an important material used in microelectronics due to its insulating properties. However, this most complex, most abundant material and widely used in optical systems is susceptible to surface alterations. Therefore, it is long being considered inappropriate for bedside healthcare applications. Yet, it is among the most important materials used in science and technology due to its robustness, chemical resistance, insulating properties and biocompatibility (Kotz et al., 2017; Geisler et al., 2019; Paget, 1924). Due to its transparency to light at telecommunication wavelengths (Arumugam, 2001; Midwinter, 1976; Palais, 1988), optical fibers composed of silica have been explored and utilized since the previous decade for light signal transfer (Suematsu, 1983; Okoshi, 1987). Despite wide usage of silica glass fibers for sensing (Chow et al., 2018; Soto et al., 2016; Caucheteur et al., 2016; Wan et al., 2015), biomedical and healthcare applications (Fried and Irby, 2018; Rao et al., 1998; Peterson and Vurek, 1984; Rao et al., 1997; Motz et al., 2004), their contribution to cancer treatment efficiency is still elusive.

Despite the wide body of research regarding optical imaging and sensing techniques for monitoring absorption changes of tumor cells
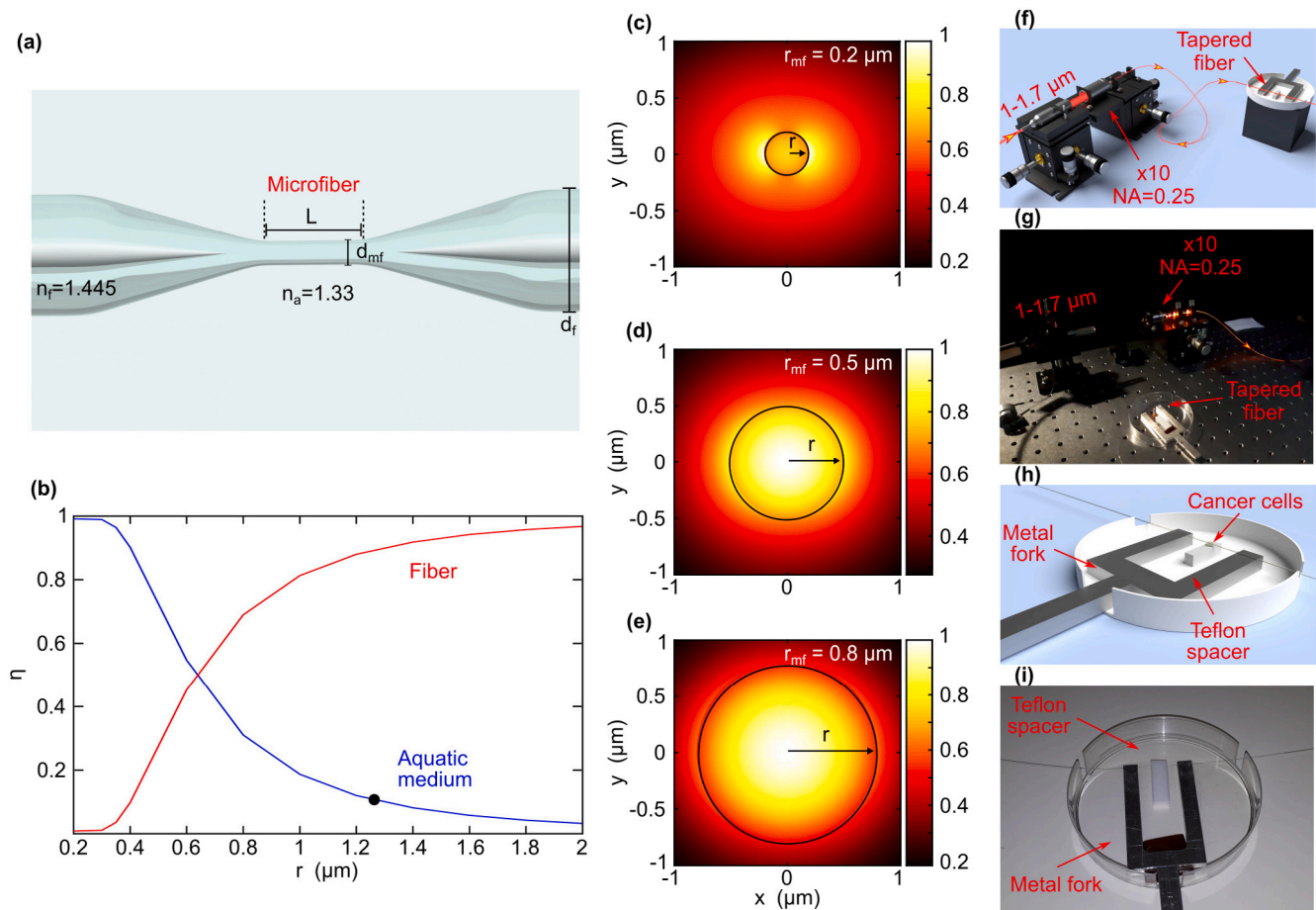
Fig. 1. Experimental set-up for overtones absorption spectroscopy from silica glass microfibers. (a) Schematic drawing of a tapered fiber structure (not to scale). (b) Calculated fraction of power at wavelength of 1.5 μm, in the fiber (red) and in the analyte (blue) with index of power of 1.33, over the total power carried by the guided modes. ~15% of the total power in the analyte is indicated by the dot. Calculated normalized electric field (EF) distributions for various microfiber radii: (c) $r_{mf} = 0.2$ μm, (d) $r_{mf} = 0.5$ μm and (e) $r_{mf} = 0.8$ μm. (f) Schematic drawing of the experimental set-up with broadband laser source coupled to a single-mode fiber using an x10 objective. (g) Photograph of the experimental setup. (h) Schematic drawing of the tapered fiber sensing device. (i) Photograph of the tapered fiber sensing device. (For interpretation of the references to color in this figure legend, the reader is referred to the web version of this article.)

(Mackanos and Contag, 2010; Chang et al., 2005; Mahadevan-Jansen et al., 1998; Sung et al., 2003) the contribution of surface topology in terms of surface roughness on optical microfibers was never explored in cancer media. For this, first we design the particular microfiber landscape by solving Maxwell equations numerically with the help of the simulator that we built, then we fabricate the microfiber, and finally, we test the microfiber in cellular media of treated and untreated cells.

In this work, we use the detection of overtone lines related to the inter-cellular cancer medium in near-infrared (NIR) in order to monitor the cancer cells treatment efficiency. Infrared spectroscopy, commonly called vibration or overtone spectroscopy, is an important analytical technique and provides information on molecular signatures in different states of matter: liquid, solid, or gas (Struve, 1989). Even though the NIR region has benefits of affordable sources and detectors developed to operate at telecommunication window, the absorption cross-section of molecular vibrations overtones is order of magnitude smaller compared to the fundamental vibrations of the same degree of freedom (Suart, 2004) making the detection of overtones at NIR spectrum challenging.

Here, we report the results of an all-optical proof-of-concept device shown on Fig. 1a for monitoring of cancer cells treatment. Based on our pioneering works on molecular vibrations overtones detection in near-infrared (NIR) (Karabchevsky and Kavokin, 2016; Katiyi and Karabchevsky, 2017, 2018; Karabchevsky et al., 2018; Dadadzhanov et al., 2018; Karabchevsky and Shalabney, 2016; Borovkova et al.,

2019; Dadadzhanov et al., 2019; Borovkova et al., 2020), we relate the absorption bands to the morphological change of cancer cells. To this end, we designed and tested the nanophotonic device to measure the overtones vibration spectra of intercellular medium of treated and untreated isolated ovarian tumor cells with different concentrations of the PI3K inhibitor. We discovered that the fingerprint signatures of the cancer cells viability could be detected from the intercellular medium. We also designed and tested the nanophotonic device to probe the overtones vibration spectrum of intercellular medium while monitoring the modification of cancer cells under selective pressure of therapy. We noticed that the enhanced evanescent field of the microfiber allows monitoring the tumors cell viability. Our results open up a plethora of precise, miniature, and portable devices for in-vitro healthcare applications and for future in-vivo applications. The bedside applications of the proposed fiber probe will involve the extraction of tumor cells from patient's ascites pre- and post-treated with chemotherapy. The efficacy of the therapy will be then monitored in-vitro with the fiber.

2. Material and methods

2.1. Fiber simulation

The fiber modes simulation was performed using COMSOL Multiphysics FEM (Finite Element Method).

2.2. Fabrication of the sensing device

We tapered the single-mode fiber (SMF-28) to approximately 2.5 μm diameter using a commercial Vytran GPX-3000 tapering system. First, we removed the acrylate polymer coating from the tapering area. The tapering was done in two step process. At the first stage the fiber was tapered from a diameter of 125 μm to a diameter of ∼15 μm. Then, the fiber was tapered from a diameter of ∼15 μm to a diameter of ∼ 2.5 μm. We glued the tapered fiber on both sides with Epoxy glue to a metal fork, which we designed and fabricated for robustness. We placed a Teflon spacer under the tapered fiber. We used the Teflon spacer as a liquid reservoir for holding the cancer cells due to the Teflon's surface tension.

2.3. Cell cycle

Cells and growth medium were collected, centrifuged for 10 mins at 4 °C, then a pellet was fixed using 70% ice-cold ethanol and stored at −20 °C. Before the read, the pellet was washed twice with cold 1X PBS, treated for 30 mins at 37 °C with 100 μl of RNase solution (100 μg/μl), and stained in the dark for 20 mins with 200 μl Propidium iodide solution (100 μg/ml). The cell phase was analyzed using BD FACSCANTO II.

2.4. Cell lines and chemical compounds

Ovarian cancer cell line (IGROV1) obtained from ATCC and maintained at 37 °C in a humidified atmosphere at 5% CO_2, in RPMI-1640 medium, supplemented with 1% L-glutamine 200 mM, 100 units of penicillin and streptomycin and 10% fetal bovine serum. GDC0032 were purchase from MedChemExpress (HY-13898) and were dissolved in DMSO at a stock concentration of 10 mM. Cell were treated at a concentration of 50 nM. The cancer cells were removed from the plastic plate by trypsin, washed in PBS and suspended in UV-sterile water at concentration of $1 \cdot 10^6$ cells/ml.

2.5. Cancer cells imaging

The cancer cells were imaged using Carl Zeiss Inverted microscope Axio Observer 7 system.

2.6. Western blotting

Plates with cells were washed with cold PBS and suspended with cold lysis buffer containing phosphatase inhibitor cocktail (Stratech, B15001-BIT). Lysates were then centrifuged at 14 000 rpm for 10 mins at 4 °C, and supernatants were collected and assayed for protein quantification using the Bradford protein assay (Biorad, 5000006). 1 mg/ml of quantified lysate were resolved on NuPAGE 4/12% Bis-Tris gels and transferred to PVDF membranes (Biorad, 1704157). Membranes were incubated for 1 h in 5% BSA in Tris-buffered saline (TBS)-Tween and then hybridized using the primary antibodies (P21, actin, AKT) in 5% BSA TBS-Tween. Horseradish peroxidase (HRP)-conjugated secondary antibodies (1:20000, GE Healthcare) were diluted in 5% BSA in TBS-Tween. Protein–antibody complexes were detected by chemiluminescence with ECL (Cyanagen) and imaged with a c300 azure camera system. SMOBIO-PM-2600 protein marker were used to analyze bend size.

2.7. Statistical analysis

The experiment was repeated at least three times. Statistical analysis was performed using GraphPad Prism software, presented as mean ± SEM. For comparisons between conditions, Ordinary one-way ANOVA were used. Values of 0.05(*), 0.01(**), 0.001(***) and 0.0001(****) were considered statistically significant.

2.8. Experiment optical set-up

A broadband laser source (Fianium WL-SC-400-8-PP), with a wavelength range from 450 nm to 2400 nm, was coupled into a SMF (1550BHP) using Olympus plan achromat objective with NA 0.25 and magnification x10. The SMF was spliced to the tapered fiber using Fujikura 70 s fiber fusion splicer. Cancer volume of 12 μL and 4000 cells/μL was dropped onto Teflon bulk and slid to the microfiber region. The transmittance spectra were collected into an optical spectrum analyzer (OSA, Yokogawa AQ6370) with a resolution of 1 nm and a sampling interval of 0.2 nm. The transmittance spectrum was measured from 1000 nm to 1700 nm.

3. Results and discussion

3.1. Numerical approach and method description

In order to find the optimal design, numerical investigations were performed before fabricating the device. The numerical model was built for the microfiber structure in which the light propagates due to the total internal reflection effect in direction of vector $\vec{k}$. The evanescent field, some fraction of the field propagated and decayed beyond the physical dimensions of the microfiber core, interacted with the studied aquatic medium. In a single-mode fiber (SMF), when the V-number is below 2.40541, only a small fraction of the power is carried in the evanescent field (Katiyi and Karabchevsky, 2017), and this affects the sensitivity of the sensor. When the V-number of the fiber is decreased, the confinement of the guided optical mode in the fiber core decreases as well (Agrawal, 2012) and more energy is guided in the cladding. Our calculations show that 70% of the power in the fiber core is guided for V-number of 2 and 20% of the power in the fiber core is guided for V-number of 1.

We designed our fibers such that the decreased confinement (Katiyi and Karabchevsky, 2017) of the optical mode increases the penetration depth of the guided light into the cellular medium by minimizing the V-number. This in turn, improved the interaction between the evanescent field and the analyte. To find the optimal fiber diameter, we calculated the fraction of the power carried by the evanescent field.

We built a simulator based on fine element method (FEM) algorithm implemented by COMSOL Multiphysics and solved Maxwell equations to study the device performance. Fig. 1b shows the fraction of the power (η) calculated according to Ref. (Katiyi and Karabchevsky, 2017) in the microfiber core and in the aquatic medium while varying the fiber radius. Fig. 1c shows the evolution of the guided modes in the fiber core as a function of the fiber radius. We notice that the smaller the diameter of the fiber, more light leaks beyond the fiber core into the medium in which the fiber is embedded. We calculated the normalized electric field distributions of a microfiber having core index of 1.445 embedded in aquatic medium with index of 1.33, for a wavelength of 1.5 μm. As the radius of the microfiber is reduced, the penetration depth of the evanescent tail increases (Fig. 1c–1e). Therefore, we fabricated a tapered fiber based on these insights; we heated and pulled an SMF with core diameter of ∼9 μm and cladding diameter of 125 μm to obtain a core diameter as small as ∼2.5 μm without a cladding. The fabricated fiber lead to an enhanced evanescent field, with ∼15% of the total power, as marked by the dot on Fig. 1b. This reduced diameter allows for efficient probing of the analyte without sacrificing the entire power.

3.2. Biological test and spectral analysis

Spectroscopic experiments were performed in biological material of seeded ovarian tumor cells, IGROV-1 (Bénard et al., 1985), on the fiber. Nine fibers (Fig. 1f), monitored using an optical spectrum analyzer (OSA, Yokogawa AQ6370), were tested. Fig. 1g shows the designed handling tool with hydrophobic Teflon spacer. A broadband laser source (Fianium WL-SC-400-8-PP) was coupled into a single-mode
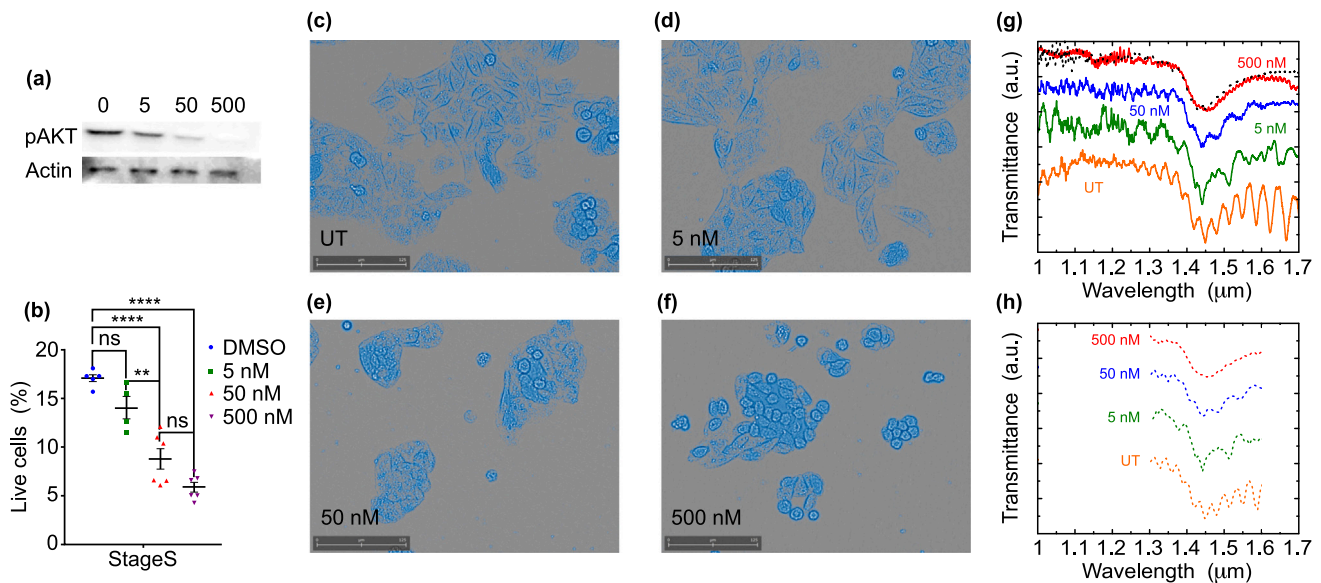
Fig. 2. (a) Western blot analysis of pAKT of IGROV-1 cells, treated with three different concentrations of GDC-0032 (5 nM, 50 nM and 500 nM) for 24 h, compared to the beta-actin level (3 repeats for each individual point). (b) Flow cytometry-based (FACS) analysis of the population in S phase in IGROV-1 cell line, 24 h after treatment with DMSO or 5 nM, 50 nM and 500 nM of GDC0032 (mean ± S.E.M. $n \geq 4$, ** $P < 0.01$, **** $P < 0.001$). Optical micrographs of IGROV1 cells: (c) untreated and treated with different medicine concentrations (d) 5 nM, (e) 50 nM, and (f) 500 nM. (g) The transmittance of cancer cells with different concentrations of the medicine. Dotted curve shows the spectral response of healthy cells. (h) Numerical modeling results for microfiber with diameter of 2.5 μm and length of 2 mm embedded in medium of different concentration of the drug. (For interpretation of the references to color in this figure legend, the reader is referred to the web version of this article.)

fiber using an objective x10. The single-mode fiber was spliced with the tapered fiber and the output spectra were collected into an optical spectrum analyzer with resolution of 1 nm. We tapered a single-mode fiber to approximately 2.5 μm diameter and glued it to a metal handling tool as shown in Fig. 1h. Since the surface of the spacer is hydrophobic and can be used a liquid-reservoir, the sample was isolated within the tear-sized dimensions on Teflon. The tumor cells in buffer solution were dripped onto the spacer and the microfiber was immersed in the droplet of 12 μL. During the experiment, the near-infrared spectrum was monitored with time intervals of 30 s to observe the time dependent change of molecular overtones signatures. In addition, we treated the IGROV-1 cells with PI3K inhibitor, GDC-0032, to explore if such agent, which is known to induce tumor growth arrest (Zorea et al., 2018), also affects the absorption of molecular overtones indicating the change in cancer viability. The sensitivity of the device to response therapy was tested by treating the IGROV-1 tumor cells with three different concentrations of GDC-0032 (5 nM, 50 nM and 500 nM) for 24 h. Using western blot (Fig. 2a) and flow cytometry (Fig. 2b) methods, we confirmed a dose-dependent effect of GDC-0032 on IGROV-1 cells with a reduction of pAKT (Abbas and Dutta, 2009) and a reduction in S phase, respectively.

Fig. 2c shows optical image of untreated cancer cells while Fig. 2d-2f show treated cancer cells with 5 nM, 20 nM and 500 nM concentration of the GDC-0032 medicine. These images show that when the concentration of the GDC-0032 increases, the cells shrink and exhibit a decrease in their spatial distribution. Following these results, we tested the NIR spectral signature of cells under the same conditions. Fig. 2g shows the transmittance of the microfiber embedded in the intercellular medium of the cancer cells while the cells were treated with 5 nM, 50 nM and 500 nM concentration of the GDC-0032 medicine. The limit of detection was determined using three standard deviations and 20 repeats of signals for each individual point. As a control signal, we measured the untreated cancer cells. The signal of untreated cancer cells shows the features of fringes related to the interference effect of relatively big bio-entities surrounding the fiber. As the concentration of the GDC-0032 on the cancer cells increases, the interference disappears but the bifurcated absorption effect appears around 1500 nm — area associated with the N–H overtone bond (Karabchevsky and Kavokin, 2016; Karabchevsky et al., 2018; Karabchevsky and Shalabney, 2016;

Wheeler, 1959). This bifurcation effect is well defined for the concentration of the GDC-0032 of 5 nM and gets suppressed when the concentration of GDC-0032 is increased to 50 nM. Related optical images show the decrease in spatial distribution of the cells as the treatment changes from 5 nM to 50 nM.

Remarkably, the dip around 1450 nm in signals obtained when the tumor was treated with 5 nM and 50 nM is associated with the hydroxylic group (Wheeler, 1959). When the concentration of the GDC-0032 is as high as 500 nM, the bifurcation merges into one well-defined and smooth dip around 1450 nm. The corresponding optical image on Fig. 2f shows that the tumor cells are squeezed and their distribution is affected, supporting our assumption that the spectral feature for 500 nM medicine concentration shows the positive response to treatment. We noticed that while further increasing the concentration of the medicine, the signal remains identical to the signals from cells treated with 500 nM GDC-0032. Therefore, we conclude that 500 nM GDC-0032 inhibits cell proliferation, and prevents the tumor growth and distribution. This inhibition affects metabolic reaction and reduces the prevalence of the N–H bonds as well as the hydroxyl groups. To understand our results, we studied the disordered wave propagation in frame of coupled-mode theory. Assuming the unperturbed system and dispersion of drug-treated and untreated (UT) medium, the translational invariance defines the waveguide modes which we solve numerically. Fig. 2h shows the numerical solution of the wave equation in cylindrical coordinates with the boundary conditions of the microfiber having a diameter of 2.5 μm and an interaction length of 2 mm embedded in different media of treated and untreated cancer cells. Numerical results are in good agreement with experimental data. We note, that in the experiment the interaction length was 4 times smaller as compared to theoretical prediction. Specifically, interaction length of the microfiber 0.5 mm was fabricated while in the theory, the interaction length was considered as 2 mm to fit the experimental data. In the experiment, 4 times enhancement in absorption is observed as compared to the theoretical estimations. This remarkable observation can be interpreted as roughness-induced absorption due to the surface roughness of the fiber discussed below.
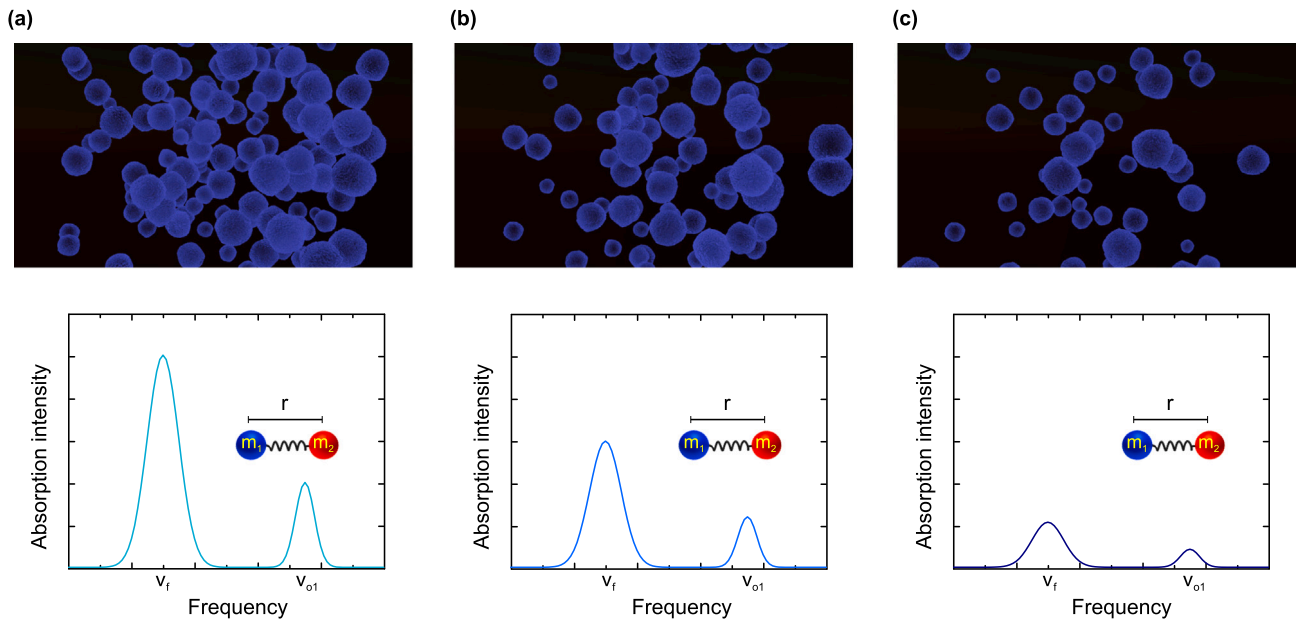
Fig. 3. Schematics of the oscillator mechanism when the cancer cells are under different treatment stages. Cellular spatial distributions (top) and the corresponding absorption intensities (bottom) for (a) low concentration of medicine, (b) medium concentration of medicine, and (c) optimal concentration of medicine — influence on cancer cells and metabolism. r designates the inter-atomic distance.

3.3. Scattering and oscillator mechanism

We note that the spatial distribution of the cancer cells has an influence on the spectral absorption signatures (Fig. 2). Fig. 2c–2f show that the concentration of the medicine during the treatment has influence on the density and distribution of the cancer cells. The cellular density affects the scattering mean free path l_{sc}, the distance until the light is scattered, which is defined as Lorenzo (2012):

$$l_{sc} = \frac{1}{\mu_s} \; [\text{cm}] \tag{1}$$

with scattering coefficient μ_s with

$$\mu_s = \rho \sigma_{sc} \tag{2}$$

where ρ is the density of the particles and σ_{sc} is the scattering cross-section of a single particle.

In untreated cancer sample, the cancer cells are densely packed (Fig. 2c) which decreases the scattering mean free path. As a result, the scattering increases, which decreases the overall-transmission as shown in Fig. 2b (orange curve). For medicine concentration of 50 nM (Fig. 2g - blue curve), the distribution of the cancer cells is small (Fig. 2e) and therefore the scattering decreases, leading to the improvement in overall transmission, and thus the molecular signature of the medium can be identified.

The oscillator mechanism when the cancer cells are under different treatment stages is shown on Fig. 3, explains how the medicine terminates the metabolism and cellular growth. When the cells are treated with insufficient concentration of medicine, they experience dense spatial distribution with well-defined cellular boundaries Fig. 3a(top). The corresponding absorption intensity of the excited overtone is as high as shown in Fig. 3a(bottom).

Fig. 3b(top) shows lower spatial density of cells as compared to Fig. 3a(top), due to the increase in the concentration of the medicine leading to suppressed absorption intensity shown in Fig. 3b(bottom). Fig. 3c shows the influence of the high concentration of the medicine on the cancer cells leading to the reduced cellular volume, lower spatial density Fig. 3c(up) and corresponding suppressed absorption lines as expected. This effect can be interpreted as the roughness-induced enhanced absorption. Recent studies show that high index nanoparticles

with high index contrast between the particles and the medium in which these particles are embedded experience directional scattering effect (Terekhov et al., 2017, 2019a,b,c; Shamkhi et al., 2019). However here, the contrast between the scatters and the medium is very low.

3.4. Enhanced absorption and surface roughness influence

It is important to note that the surface roughness plays a crucial role in the observed effect of roughness-induced enhanced absorption. Ideally, the optical fiber is considered as having a smooth surface, also tapered fibers illuminated with external source show continuous and smooth boundary as shown in Fig. 4a (captured with x100 home-built magnification system). However, the heating-based tapering process, introduces surface roughness. To explore the effect of surface roughness, we switched off the external free-space illumination in home-built magnification system and coupled the light into the tapered fiber itself. Now, when the tapered fiber guides a light, the bright scattered spots can be observed (Fig. 4b). This is the evidence that the unbounded glass surface has a random surface roughness.

The surface roughness of the microfiber can be represented as a variation in the microfiber core radius. In the first approximation, the microfiber surface roughness can be explained by the Gaussian random field. The perturbation magnitude can vary and therefore, the amplitude of the electric field in guided and radiated modes changes contributing altogether to the surface sensitivity. The spectral power density $P(k)$ of the surface roughness can be expressed as Jackle and Kawasaki (1995):

$$P(k) = \frac{k_B T}{\alpha |k|^2} \tag{3}$$

where T is the glass transition temperature, α is the surface tension in the transition, and k is the countradirectional wave vector. The lower cut-off wavevector is $\sqrt{gd/\alpha}$, where d is the glass density. Now, the surface roughness can be defined in terms of roughness variance and power density

$$\sigma^2 = \frac{1}{2\pi^2} \int_{-\infty}^{\infty} P(k) \, d^2 k \tag{4}$$
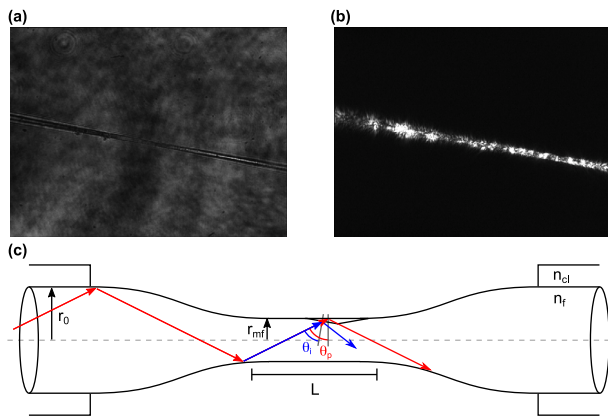
Fig. 4. In-house x100 optical microscope image of fabricated microfiber illuminated with (a) external light source and (b) guided light in the fiber itself while the external light source was switched off. (c) Model diagram of ray propagation inside the core of optical microfiber. The red arrow shows the ray bounced in between the smooth fiber walls. θ_p is the angle with fiber boundary for microfiber with continuous smooth boundary while the blue arrow shows the ray bounced in between the rough fiber walls (θ_i). (For interpretation of the references to color in this figure legend, the reader is referred to the web version of this article.)

In the single mode operation of the glass microfiber, the spectral components $P(k)$ are considerably large and therefore, they are responsible to enlarge the evanescent fields, which in turn contribute to the surface sensitivity of our device.

The surface roughness of the microfiber has a significant influence on the evanescent field. For smooth fiber, the wave propagates in θ_p due to the effect of total internal reflection (TIR). However, in case of rough fiber, the angle at which the ray hits the fiber boundary is different than the propagating angle (Fig. 4c). The boundary incident angle θ_i is influenced by the roughness of the surface and is defined as Zhong et al. (2013):

$$\theta_i = \theta_p - \tan^{-1}\left(\frac{2\delta}{\Delta}\right) \tag{5}$$

where θ_p is the propagating angle for smooth fiber with continuous boundary, δ is the average pit depth, and Δ is the average pit diameter as shown in Fig. 4c.

Eq. (5) shows that the incident angle θ_i is a function of fiber roughness. In addition, the change in θ_i has an influence on the penetration depth d_p of the evanescent field into the cellular medium as it is defined in Eq. (6) as the distance for which the field intensity decays to 37% ($1/e$) compared to the field intensity at the guiding layer boundary. The penetration depth is defined as:

$$d_p = \frac{\lambda}{2\pi\sqrt{n_f{}^2 \sin^2(\theta_i) - n_a{}^2}} \tag{6}$$

where n_a is the refractive index for the analyte, n_f is the refractive index for the fiber and θ_i is the incident angle. Eq. (6) emphasizes that the penetration depth depends on the incident angle. The smaller the incident angle, the larger the penetration of the evanescent field into the cellular medium which, in turn, improves the sensitivity of the device.

4. Conclusions

We found that the treatment of tumor cells with GDC0032, a beta-sparing PI3K, induced both growth arrest and altered the spectral lines in a dose-dependent manner. We interpreted the observed effect in terms of the roughness-induced absorption of light mediated by surface scatterers. Enhancement in absorption as high as 4 times was observed as compared to the theoretical estimations. This remarkable enhancement is interpreted by means of the roughness-induced absorption

resulting in increased interaction length due to the microfiber surface roughness. We explained the role of the surface roughness in the observed spectral effect. The monitoring method for treatment efficiency of ovarian cancer based on a microfiber device demonstrated here has several advantages compared to the conventional techniques involving the positron emission tomography (PET) and an X-ray computed tomography (CT). Importantly, the guided-light microfiber device does not involve irradiation of the patient, it is suitable for bedside applications, and gives real-time spectral response. Our findings form an essential step toward the development of early detection of response to cancer therapy. The simplicity of our approach opens a window for further in-vitro clinical investigation also for many accessible cancers such as esophageal, colorectal, cervical. In the future we aim at developing this system for in-vivo applications also suitable for lower acceptable such as brain cancers. This will consist the engineered biocompatible cage-jacket encapsulating fragile sensing area to monitor tumors in-vivo.

Declaration of competing interest

The authors declare that they have no known competing financial interests or personal relationships that could have appeared to influence the work reported in this paper.

CRediT authorship contribution statement

Aviad Katiyi: Investigation, Visualization, Methodology. **Jonathan Zorea:** Investigation, Resources. **Aviran Halstuch:** Investigation, Resources. **Moshe Elkabets:** Investigation, Supervision. **Alina Karabchevsky:** Investigation, Supervision, Conceptualization.

Acknowledgments

References

Abbas, T., Dutta, A., 2009. P21 in cancer: intricate networks and multiple activities. Nat. Rev. Cancer 9 (400).

Agrawal, G.P., 2012. Fiber-Optic Communication Systems, vol. 222. John Wiley & Sons.

Arumugam, M., 2001. Optical fiber communication—an overview. Pramana 57, 849–869.

Bénard, J., D. Silva, J., D. Blois, M.C., Boyer, P., Duvillard, P., Chiric, E., Riou, G., 1985. Characterization of a human ovarian adenocarcinoma line, igrov1, in tissue culture and in nude mice. Cancer Res. 45, 4970–4979.

Beyer, T., Townsend, D.W., Brun, T., Kinahan, P.E., Charron, M., Roddy, R., Jerin, J., Young, J., Byars, L., Nutt, R., et al., 2000. A combined pet/ct scanner for clinical oncology. J. Nucl. Med. 41, 1369–1379.

Borovkova, O., Ignatyeva, D., Sekatskii, S., Karabchevsky, A., Belotelov, V., 2019. High-q surface electromagnetic wave resonance excitation in magneto-photonic crystals for super-sensitive detection of weak light absorption in near-ir. ArXiv preprint arXiv:1910.11406.

Borovkova, O., Ignatyeva, D., Sekatskii, S., Karabchevsky, A., Belotelov, V., 2020. High-q surface electromagnetic wave resonance excitation in magnetophotonic crystals for supersensitive detection of weak light absorption in the near-infrared. Photonics Res. 8, 57–64.

Caucheteur, C., Guo, T., Liu, F., Guan, B.O., Albert, J., 2016. Ultrasensitive plasmonic sensing in air using optical fibre spectral combs. Nat. Commun. 7 (13371).

Chang, S.K., Mirabal, Y.N., Atkinson, E.N., Cox, D.D., Malpica, A., Follen, M., Richards-Kortum, R.R., 2005. Combined reflectance and fluorescence spectroscopy for in vivo detection of cervical pre-cancer. J. Biomed. Opt. 10, 024031.

Chow, D.M., Yang, Z., Soto, M.A., Thévenaz, L., 2018. Distributed forward brillouin sensor based on local light phase recovery. Nat. Commun. 9 (2990).

Dadadzhanov, D.R., Vartanyan, T.A., Karabchevsky, A., 2018. Vibrational overtones spectroscopy enabled by plasmonic nanoantennas. In: Plasmonics: Design, Materials, Fabrication, Characterization, and Applications XVI. International Society for Optics and Photonics, p. 107222E.

Dadadzhanov, D.R., Vartanyan, T.A., Karabchevsky, A., 2019. Differential extinction of vibrational molecular overtone transitions with gold nanorods and its role in surface enhanced near-ir absorption (senira). Opt. Express 27, 29471–29478.

Fischer, B., Lassen, U., Mortensen, J., Larsen, S., Loft, A., Bertelsen, A., Ravn, J., Clementsen, P., Høgholm, K., et al., 2009. Preoperative staging of lung cancer with combined pet–ct. New Engl. J. Med. 361, 32–39.

Fishman, D.A., Bozorgi, K., 2002. The scientific basis of early detection of epithelial ovarian cancer: the national ovarian cancer early detection program (nocedp). In: Ovarian Cancer. Springer, pp. 3–28.

Fried, N.M., Irby, P.B., 2018. Advances in laser technology and fibre-optic delivery systems in lithotripsy. Nat. Rev. Urol. 15, 563–573.

Geisler, T., Dohmen, L., Lenting, C., Fritzsche, M.B., 2019. Real-time in situ observations of reaction and transport phenomena during silicate glass corrosion by fluid-cell raman spectroscopy. Nat. Mater. 18 (342).

Jackle, J., Kawasaki, K., 1995. Intrinsic roughness of glass surfaces. J. Phys.: Condens. Matter 7 (4351).

Johnson, P., Federico, M., Kirkwood, A., Fosså, A., Berkahn, L., Carella, A., d'Amore, F., Enblad, G., Franceschetto, A., Fulham, M., et al., 2016. Adapted treatment guided by interim pet-ct scan in advanced hodgkin's lymphoma. New Engl. J. Med. 374, 2419–2429.

Karabchevsky, A., Katiyi, A., Bin Abdul Khudus, M.I.M., Kavokin, A.V., 2018. Tuning the near-infrared absorption of aromatic amines on tapered fibers sculptured with gold nanoparticles. ACS Photonics 5, 2200–2207.

Karabchevsky, A., Kavokin, A., 2016. Giant absorption of light by molecular vibrations on a chip. Sci. Rep. 6 (21201).

Karabchevsky, A., Shalabney, A., 2016. Strong interaction of molecular vibrational overtones with near-guided surface plasmon polariton. In: Optical Sensing and Detection IV. International Society for Optics and Photonics, p. 98991T.

Katiyi, A., Karabchevsky, A., 2017. Figure of merit of all-dielectric waveguide structures for absorption overtone spectroscopy. J. Lightwave Technol. 35, 2902–2908.

Katiyi, A., Karabchevsky, A., 2018. Si nanostrip optical waveguide for on-chip broadband molecular overtone spectroscopy in near-infrared. ACS Sensors 3, 618–623.

Kotz, F., Arnold, K., Bauer, W., Schild, D., Keller, N., Sachsenheimer, K., Nargang, T.M., Richter, C., Helmer, D., Rapp, B.E., 2017. Three-dimensional printing of transparent fused silica glass. Nature 544 (337).

Kurian, A.W., Sigal, B.M., Plevritis, S.K., 2010. Survival analysis of cancer risk reduction strategies for brca1/2 mutation carriers. J. Clin. Oncol. 28, 222.

Lee, J., Ledermann, J., Kohn, E., 2013. Parp inhibitors for brca1/2 mutation-associated and brca-like malignancies. Ann. Oncol. 25, 32–40.

Lengyel, E., 2010. Ovarian cancer development and metastasis. Am. J. Pathol. 177, 1053–1064.

Lorenzo, J.R., 2012. Principles of Diffuse Light Propagation: Light Propagation in Tissues with Applications in Biology and Medicine. World Scientific.

Mackanos, M.A., Contag, C.H., 2010. Fiber-optic probes enable cancer detection with ftir spectroscopy. Trends Biotechnol. 28, 317–323.

Mahadevan-Jansen, A., Mitchell, M.F., Ramanujam, N., Utzinger, U., Richards-Kortum, R., 1998. Development of a fiber optic probe to measure nir raman spectra of cervical tissue in vivo. Photochem. Photobiol. 68, 427–431.

Midwinter, J., 1976. Trends in optical fibre transmission research. Nature 261 (371).

Motz, J.T., Hunter, M., Galindo, L.H., Gardecki, J.A., Kramer, J.R., Dasari, R.R., Feld, M.S., 2004. Optical fiber probe for biomedical raman spectroscopy. Appl. Opt. 43, 542–554.

Noone, A., Howlader, N., Krapcho, M., Miller, D., Brest, A., Yu, M., Ruhl, J., et al., 2018. Seer Cancer Statistics Review, 1975–2015, Based on November 2017 Seer Data Submission, Posted To the Seer Web Site, April 2018. National Cancer Institute, Bethesda, MD.

Okoshi, T., 1987. Recent advances in coherent optical fiber communication systems. J. Lightwave Technol. 5, 44–52.

Paget, R., 1924. Fused silica.

Palais, J.C., 1988. Fiber Optic Communications. Prentice Hall, Englewood Cliffs.

Pelosi, E., Messa, C., Sironi, S., Picchio, M., Landoni, C., Bettinardi, V., Gianolli, L., De Maschio, A., Gilardi, M.C., Fazio, F., 2004. Value of integrated pet/ct for lesion localisation in cancer patients: a comparative study. Eur. J. Nucl. Med. Mol. Imaging 31, 932–939.

Peterson, J.I., Vurek, G.G., 1984. Fiber-optic sensors for biomedical applications. Science 224, 123–127.

Rao, Y.J., Webb, D.J., Jackson, D.A., Zhang, L., Bennion, I., 1997. In-fiber bragg-grating temperature sensor system for medical applications. J. Lightwave Technol. 15, 779–785.

Rao, Y.J., Webb, D., Jackson, D.A., Zhang, L., Bennion, I., 1998. Optical in-fiber bragg grating sensor systems for medical applications.

Schäfers, K.P., Stegger, L., 2008. Combined imaging of molecular function and morphology with pet/ct and spect/ct: image fusion and motion correction. Basic Res. Cardiol. 103, 191–199.

Shamkhi, H.K., Baryshnikova, K.V., Sayanskiy, A., Kapitanova, P., Terekhov, P.D., Belov, P., Karabchevsky, A., Evlyukhin, A.B., Kivshar, Y., Shalin, A.S., 2019. Transverse scattering and generalized kerker effects in all-dielectric mie-resonant metaoptics. Phys. Rev. Lett. 122, 193905.

Soto, M.A., Ramirez, J.A., Thevenaz, L., 2016. Intensifying the response of distributed optical fibre sensors using 2d and 3d image restoration. Nat. Commun. 7 (10870).

Stegger, L., Juergens, K.U., Kliesch, S., Wormanns, D., Weckesser, M., 2007. Unexpected finding of elevated glucose uptake in fibrous dysplasia mimicking malignancy: contradicting metabolism and morphology in combined pet/ct. Eur. Radiol. 17 (1784).

Struve, W.S., 1989. Fundamentals of Molecular Spectroscopy. Wiley, New York.

Suart, B., 2004. Infrared Spectroscopy: Fundamental and Applications. John Wiley & Sons, Ltd.

Suematsu, Y., 1983. Long-wavelength optical fiber communication. Proc. IEEE 71, 692–721.

Sung, K.B., Richards-Kortum, R., Follen, M., Malpica, A., Liang, C., Descour, M.R., 2003. Fiber optic confocal reflectance microscopy: a new real-time technique to view nuclear morphology in cervical squamous epithelium in vivo. Opt. Express 11, 3171–3181.

Terekhov, P.D., Babicheva, V.E., Baryshnikova, K.V., Shalin, A.S., Karabchevsky, A., Evlyukhin, A.B., 2019a. Multipole analysis of dielectric metasurfaces composed of nonspherical nanoparticles and lattice invisibility effect. Phys. Rev. B 99, 045424.

Terekhov, P.D., Baryshnikova, K.V., Artemyev, Y.A., Karabchevsky, A., Shalin, A.S., Evlyukhin, A.B., 2017. Multipolar response of nonspherical silicon nanoparticles in the visible and near-infrared spectral ranges. Phys. Rev. B 96, 035443.

Terekhov, P.D., Baryshnikova, K.V., Greenberg, Y., Fu, Y.H., Evlyukhin, A.B., Shalin, A.S., Karabchevsky, A., 2019b. Enhanced absorption in all-dielectric metasurfaces due to magnetic dipole excitation. Sci. Rep. 9 (3438).

Terekhov, P., Shamkhi, H., Gurvitz, E., Baryshnikova, K., Evlyukhin, A., Shalin, A., Karabchevsky, A., 2019c. Broadband forward scattering from dielectric cubic nanoantenna in lossless media. Opt. Express 27, 10924–10935.

Wan, N.H., Meng, F., Schröder, T., Shiue, R.J., Chen, E.H., Englund, D., 2015. High-resolution optical spectroscopy using multimode interference in a compact tapered fibre. Natu. Commun. 6 (7762).

Wheeler, O.H., 1959. Near infrared spectra of organic compounds. Chem. Rev. 59, 629–666.

Zhong, N., Zhu, X., Liao, Q., Wang, Y., Chen, R., Sun, Y., 2013. Effects of surface roughness on optical properties and sensitivity of fiber-optic evanescent wave sensors. Appl. Opt. 52, 3937–3945.

Zorea, J., Prasad, M., Cohen, L., Li, N., Schefzik, R., Ghosh, S., Rotblat, B., Brors, B., Elkabets, M., 2018. Igf1r upregulation confers resistance to isoform-specific inhibitors of pi3k in pik3ca-driven ovarian cancer. Cell Death Dis. 9 (944).